HENRY

Hydraulic Engineering Repository

Ein Service der Bundesanstalt für Wasserbau

Conference Paper, Published Version

Davis, Mastaneh; Koenders, M. A.; Köhler, Hans-Jürgen

Pore pressure response due to turbulent flow patterns using combined lattice Boltzmann and analytical methodology (Bestimmung von Porenwasserdruckreaktionen initialisiert durch turbulente Strömungsmuster unter Anwendung einer Kombination aus Lattice-Boltzmann Simulation und analytischer Berechnungs-methodik)

10 Pore pressure response due to turbulent flow patterns using combined lattice Boltzmann and analytical methodology

Bestimmung von Porenwasserdruckreaktionen initialisiert durch turbulente Strömungsmuster unter Anwendung einer Kombination aus Lattice-Boltzmann Simulation und analytischer Berechnungsmethodik

M. Davis & M. A. Koenders

Kingston University, Department of Mathematics, Kingston on Thames, UK
Kingston Universität, Abteilung für Mathematik, Kingston on Thames, UK

H.-J. Köhler

Bundesanstalt für Wasserbau, Abteilung Geotechnik, Karlsruhe, Germany
Federal Waterways Engineering and Research Institute, Geotechnical Department, Karlsruhe, Germany

ABSTRACT: Lattice-Boltzmann simulations have been used to calculate flow patterns over and inside a gravel bed, which in turn rests on sandy subsoil. The resulting flow pressure profile has been employed to obtain the excess pore pressure in the subsoil; both the temporal and spatial developments have been evaluated by means of an analytical solution of Biot's equations for partially saturated soil. Using the analysis one is able to ascertain the location of most likely damage in the subsoil of a river or sea bed. The effect of an obstacle in the flow is examined and the presence of such an object has non-negligible consequences for the potential damage assessment.

KURZFASSUNG: Die Methode der Lattice-Boltzmann Simulation wurde benutzt, um Strömungsmuster oberhalb und innerhalb eines Kiesbettes zu bestimmen, das auf einem sandigen Untergrund liegt. Die aus der Durch- und Überströmung resultierenden Wasserdruckprofile wurden als Eingangsgrößen für die Bestimmung der im unterlagernden Sand initialisierten Porenwasserüberdrücke angesetzt. Sowohl die zeitlich als auch räumlich veränderlichen Porenwasserdruckentwicklungen konnten analytisch mit Hilfe der Konsolidations-Gleichung von Biot für den teilgesättigten Sand unter Wasser berechnet werden. Die Anwendung einer solchen Analyse hilft, mögliche Schadenspotentiale hinsichtlich seines örtlichen Auftretens im Untergrund eines Gewässerbettes zu bestimmen. Die Einflüsse von Strömungshindernissen oberhalb des Kiesbettes auf die möglichen Schadenspotentiale im Untergrund und an der Gewässersohle sind nach den Ergebnissen dieser Untersuchung keinesfalls vernachlässigbar.

10.1 Introduction

This paper is concerned with the analysis of rip-rap-protected, non-cohesive sand layers subjected to flow conditions tha3t are non-uniform, both in a temporal and in a spatial sense. The temporal non-uniformity is associated either with 'turbulence' in the mean flow outside the rip rap layers, or with explicit time-dependent loading due to wave action. The spatial non-uniformity may also be due to wave loading (the wave length being much greater than the mean size of the protective granular layer), but arises chiefly as a result of obstacles in the extraneous flow. The design of stable rip rap layers is treated in the literature /Raudkivi 1998/ (see section 9.10 for an overview). The sand layer underneath the protective layer is usually deemed to be stable if the protective filter layer is stable and the ratio of the sizes of the base material to the filter material satisfies Terzaghi's conditions /Terzaghi 1943/. Alternatively geotextiles may be employed, especially for temporary structures. The thickness of the filter is designed in such a way that in a geometrical sense Terzaghi's rules make sense, which in practice comes down to some 0.2 metres for gravel filters. Size segregation during deposition is generally viewed as undesirable.

The question now is what happens when the rip rap cannot be used in such a way that Terzaghi's geometrical filter conditions are satisfied. The gravel will still have a protective function in that it moderates the flow over the sandy subsoil, yet - potentially - erosion of the non-cohesive sand may take place if flow conditions in the pores of the deposited rip rap are sufficiently severe. In a naïve analysis then, the flow conditions in the pores need to be analysed and if the local flow conditions (tangential to the filter/base interface) exceed the critical conditions /Raudkivi 1998/ (see chapter 3) instability and subsequent erosion may be expected. This analysis is naïve because it only tells part of the story and overlooks an important mechanism: the combined effect of small amounts of gas in the subsoil and temporal pressure variations.

The notion that gas in the subsoil may affect the erosion susceptibility of a non-cohesive soil has been explored in a recent paper /Köhler & Koenders 2003/. In the theoretical part of this paper a partially saturated sandy half-space is loaded by an external pressure fall. Using Biot's equations /Biot 1941/ the pressure profile in the half-space is calculated. It transpires that even in a slightly unsaturated environment fluidisation may take place if the external pressure goes on falling for long enough. In the experimental part of the paper it is shown by means of an endoscopic technique that the gas is present in bubble form; the bubbles adhere to the sand grains and are virtually indestructible. During the external pressure fall they expand; the fluidisation, when it takes place, is also verified with the use of endoscopy.

The theory predicts that fluidisation of an unprotected bed first takes place after a time t_1 reckoned from the moment when the external pressure had started to fall at a rate of $\dot{\sigma}$. An estimate of t_1 is a key design parameter for unprotected beds. Basically, it states: if one expects the external pressure fall at a rate $\dot{\sigma}$ to continue for less than a period of t_1, then the bed will not fluidise. If it goes on for a period of time that is greater than t_1, then fluidisation will occur. The estimate for the time t_1 is

$$t_1 = \pi Y \left(\frac{i_c \gamma_w}{\dot{\sigma} a} \right)^2 \tag{10-1}$$

where Y is the pressure-equivalent water depth, the critical gradient /Terzaghi 1943/ (measured in engineering units as a fraction of the fluid specific weight γ_w) and a a system parameter with the dimension of the inverse of the square root of a velocity. The latter is the only variable that contains information about the particle/fluid/gas mixture. The presence of the gas bubbles is represented through the saturation measure, s_i, stating the fraction of the fluid that is not in bubble form. Note that the bubbles tend to adhere to the grains; in fact it is very difficult to get rid of them and a typical figure for the saturation in natural deposits at water depths that are less than 10 m deep is some 95-99%. The saturation is embedded in the parameter a as follows

$$a^2 = \frac{4n(1 - s_i)}{k} \tag{10-2}$$

where n is the porosity of the deposit and k its permeability.

Protection of the subsoil can be introduced by means of a layer of a coarse, more permeable material. The analysis and design of the thickness of the layer has been discussed by /Roussell et al 2000/. In this case the whole system fails due to the mechanism that involves gas in the subsoil and not local failure in the pores of the protective layer. This analysis is also one-dimensional.

The geometry of the half-space analysis is naturally limited; its importance lies in the introduction of the concepts, though direct application is possible, for example in locks. In this paper the analysis is extended to include both another important engineering geometry as well as external pressure fluctuations that arise from a time-dependent flow field. The latter may result from either continuous flow over an obstacle or from explicit wave-loading, or – in principle – a combination of these two.

In order to illustrate the problem Bild 10.1 is helpful. A rigid, impermeable obstacle has been placed on a coarse gravel layer; the latter protects a non-

cohesive, partially saturated subsoil. Flow is applied to the outer regions of the conformation. The approach that is taken to study these problems is as follows. The flow in the open water and in the coarse layer is modelled in two dimensions by means of a lattice-Boltzmann technique. This technique is particularly suited to the highly irregular boundaries that result from the gravel material. At the same time this technique can cope with the wide variety of flow conditions that appear in this problem: the typical Reynolds number in the open water is very much higher than the one that reigns in the flow in the rip-rap. The flow in the subsoil is not simultaneously modelled by the lattice-Boltzmann technique. In the sandy region the boundary conditions from the flow modelling are used to calculate the excess pore pressures analytically. Due consideration is given to the presence of gas.

The purpose of the calculations is to establish the regions in which damage is most likely. Erosion may be associated with the two mechanisms: high interfacial tangential fluid velocities or with local fluidisation due to gas in the subsoil in the sand. A combination of both is naturally also possible. In this paper the first mechanism is not further explored, because – as mentioned above – there is already much literature on erosion due to high tangential flows.
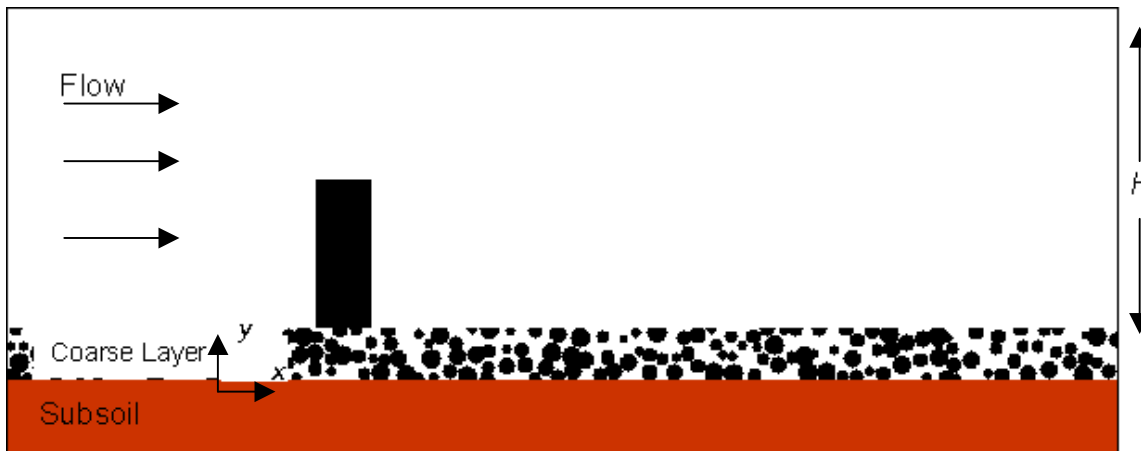
$$\frac{k}{\gamma_w}\left(\frac{\partial^2 p}{\partial x^2} + \frac{\partial^2 p}{\partial y^2}\right) = \left[\frac{n(1-s_i)}{p_0}\right]\frac{\partial p}{\partial t} \qquad (10\text{-}3)$$

Here k is the soil permeability, n the porosity and γ_w the specific weight of fluid (water); p_0 is the mean ambient pressure near the top of the subsoil.

The position is identified by the horizontal co-ordinate x and the vertical co-ordinate y. The saturation is denoted by s_i and is assumed to be a constant, independent of time and position. The equation is valid for fine-grained soils in which the fluid flow is laminar. The further crucial approximation that has been made is that the stiffness of the soil is much greater than the stiffness of the fluid-gas mixture. This can only be true under unsaturated circumstances, but that is the limit considered here. As a rule of thumb the approximation is true for dense non-cohesive soils with gas content in the fluid > 1%.

For convenience a parameter A is introduced as

$$A \equiv \frac{k}{\gamma_w}\frac{p_0}{n(1-s_i)}. \qquad (10\text{-}4)$$

This parameter has the dimension of $m^2 s^{-1}$ and

Bild 10.1   Geometry of the problem. The thickness of the coarse layer is y_0

The analysis is part of a wider research exercise. In this paper the analysis is demonstrated. In a forthcoming paper a series of experiments will be reported, as well as variations of the calculations.

10.2 Estimate of the pressure gradient of a loaded half-space

It was demonstrated by /Köhler & Koenders 2003/ that for a partially saturated subsoil under shallow conditions, the excess pore pressure development $p(x,y,t)$ as a function of position and time is approximately described by the following equation

plays the role of consolidation coefficient.

Equation (10-3) with the definition of the parameter A gives

$$A\left(\frac{\partial^2 p}{\partial x^2} + \frac{\partial^2 p}{\partial y^2}\right) = \frac{\partial p}{\partial t} \qquad (10\text{-}5)$$

A Fourier transform (denoted by a ^) of the equation with respect to the x-co-ordinate with Fourier wave number χ is applied to give equation (10-5), and gives:

$$A(-\chi^2 \hat{p} + \frac{\partial^2 \hat{p}}{\partial y^2}) - \frac{\partial \hat{p}}{\partial t} = 0 . \qquad (10\text{-}6)$$

A Laplace transform with respect to t is performed with frequency s; the transformed variable is denoted by a ~

$$A\left(-\chi^2 \widetilde{\hat{p}} + \frac{\partial^2 \widetilde{\hat{p}}}{\partial y^2}\right) - s\widetilde{\hat{p}} + \hat{p}(\chi,y,t=0) = 0 . \quad (10\text{-}7)$$

The initial excess pore pressure in the process is zero and therefore the last term on the left-hand side vanishes. Equation (10-7) represents an ordinary linear differential equation. The excess pore pressure gradient vanishes for very large values of -y (no flow at great depth) and therefore the solution is

$$\widetilde{\hat{p}} = \widetilde{\hat{p}}(\chi, y=0, s) e^{y\sqrt{\chi^2 + s/A}} . \qquad (10\text{-}8)$$

Applying the convolution theorem for both Laplace and Fourier transform the excess pore pressure field is obtained as

$$p(x,y,t) = \int_0^t d\tau \int_{-\infty}^{+\infty} d\xi \, p(x-\xi,0,t-\tau) L^{-1}\left[F^{-1}\left(e^{y\sqrt{\chi^2+s/A}}\right)\right](\xi,\tau)$$

$$(10\text{-}9)$$

Both the inverse Laplace and Fourier transforms are easily carried out /Abramowitz & Stegun 1965/, (29.2.12, 29.3.82); /Gradshteyn & Ryzhik 2000/, (3.922.4) to give

$$p(x,y,t) = \frac{-y}{4A\pi} \int_0^t d\tau \int_{-\infty}^{+\infty} d\xi \, p(x-\xi,0,t-\tau) \frac{1}{\tau^2} e^{-\frac{y^2+\xi^2}{4A\tau}} . $$

$$(10\text{-}10)$$

The excess pore pressure at $y = 0$ needs to be given for all horizontal positions and time points. This quantity is supplied by the numerical lattice-Boltzmann solution in the open water and in the coarse layer.

The form of formula (10-10) is suitable for numerical implementation for $y \neq 0$. For y in the vicinity of zero change the integration variable ζ to $\zeta \equiv 4A\tau/y^2$. The integral of Equation (10-10) then reads

$$p(x,y,t) = \lim_{y \uparrow 0} \frac{-1}{\pi y} \int_0^{4At/y^2} d\zeta \int_{-\infty}^{+\infty} d\xi \, p\left(x-\xi, 0, t - \frac{y^2 \zeta}{4A}\right) \frac{1}{\zeta^2} e^{-\frac{1}{\zeta}\left(1+\frac{\xi^2}{y^2}\right)} .$$

$$(10\text{-}11)$$

The integration over y is dominated by the region in the vicinity of $\zeta = 0$ due to the presence of the term $1/\zeta^2$; therefore in the vicinity of $y \approx 0$ the

argument $t - y^2 \zeta /(4A) \approx t$. The integral over τ is now carried out to give

$$p(x,y,t) = \lim_{y \uparrow 0} \frac{-1}{\pi} \int_{-\infty}^{+\infty} d\xi \, p(x-\xi,0,t) \frac{ye^{-\frac{y^2+\xi^2}{4At}}}{y^2 + \xi^2} .$$

$$(10\text{-}12)$$

The integrand is zero for all $\xi \neq 0, y \uparrow 0$ and therefore it is only necessary to investigate the result in the vicinity of $\xi = 0$ and here $p(x-\xi,0,t) \approx p(x,0,t)$. Thus, using /Gradsheyn & Ryzhik 2000/, (see section 3.466)

$$p(x,y,t) = p(x,0,t) \lim_{y \uparrow 0} \frac{-1}{\pi} \int_{-\infty}^{+\infty} d\xi \frac{ye^{-\frac{y^2+\xi^2}{4At}}}{y^2 + \xi^2} \quad (10\text{-}13 \text{ a})$$

$$p(x,y,t) = 2p(x,0,t) \lim_{(-y) \downarrow 0} \frac{1}{\pi} \int_0^{+\infty} d\xi \frac{(-y)e^{-\frac{y^2+\xi^2}{4At}}}{y^2 + \xi^2} = p(x,0,t).$$

$$(10\text{-}13 \text{ b})$$

This is the expected result.

For the numerical equivalent of Equation (10-10) is

$$p(x,y,t) = \frac{-y}{4\pi A} \sum_{j=1}^{M} \sum_{i=1}^{N} p(x-\xi_i,0,t-\tau_j) \frac{1}{\tau_j^2} e^{-\left(y^2+\xi_i^2\right)/\left(4A\tau_j\right)},$$

$$(10\text{-}14)$$

where N is the number of spatial points along the interface, M the number of the temporal points. The excess pore pressure at the interface must be given as a function of both position and time. This function is supplied by the lattice-Boltzmann simulation.

10.3 The lattice Boltzmann method for the computation of fluid flow

The simulation of the flow in both the open water and the coarse layer regions is performed with the lattice Boltzmann method. This method is especially appropriate for the highly irregular boundary conditions that are present in the coarse layer. There is a wealth of literature on the method, which may be employed in a diverse range of applications: fluid flow, flows in complex geometries, multiphase and multicomponent flows, particles in fluids, heat transfer and reaction-diffusion. Here a brief discussion is included pertaining to the basics of the method; especially the scaling rules for physical parameters in fluid flow and specification of the boundary conditions are mentioned. Overview

publications on the subject are /Chen & Doolen 1998/, /Chopard & Droz 1999/ and /Succi 2001/.

In the lattice Boltzmann method the physical quantities of interest are described in terms of $\overline{N}$ fields $f_i(\boldsymbol{r},t)$ ($i = 1...\overline{N}$) defined at each point r of a lattice and at each discrete time step t. In hydrodynamic applications the fields represent fluid particle numbers. The fluid particles may have velocities; these are classified in a discrete set of possibilities in both size and direction and the subscript i refers to a possible velocity direction. By way of illustration a two-dimensional lattice is shown in Bild 10-2. This is a square lattice; the 8 unit vectors e_i point to the nearest neighbour in direction i. Fluid particles may move along any of these unit vectors.
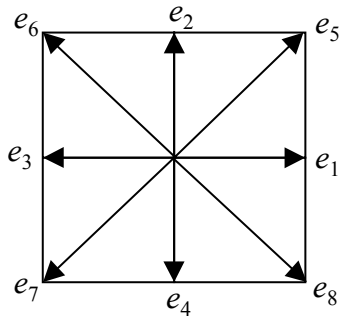

Bild 10.2   *The eight unit vectors e_i pointing to the nearest neighbouring site in direction i.*

The next step is to consider evolution in the fluid particle numbers. There are two contributing factors to the change in the number of particles at any grid point. The first is free convection, stating

$$f_i(\boldsymbol{r} + \mathbf{e}_i, t+1) = f_i(\boldsymbol{r}, t) \qquad (10\text{-}15)$$

The lattice spacing and the time increment are most conveniently chosen to be equal to unity. Equation (10-15) allows particles moving in the same direction to occupy the same lattice site at the same time. This leads to unphysical results and therefore an exclusion principle needs to be applied. To deal with this problem particles are allowed to collide on the lattice; this feature is introduced in the second element of the evolution process, a collision operator Ω, the modified evolution equation then reads

$$f_i(\boldsymbol{r} + \mathbf{e}_i, t+1) - f_i(\boldsymbol{r}, t) = \Omega_i(\boldsymbol{r}, t) \qquad (10\text{-}16)$$

The function f_i is the mesoscopic particle distribution, which is the ensemble average of the particle occupation. Furthermore, it is assumed that the collision operator only depends on the incoming particle distribution /Chen & Doolen 1998/; the evolution equation then becomes the so-called lattice-Boltzmann equation

$$f_i(\boldsymbol{r} + \mathbf{e}_i, t+1) - f_i(\boldsymbol{r}, t) = \Omega_i(f_i) \qquad (10\text{-}17)$$

Once the collision operator is specified, the rule is completely local and easy to compute. The macroscopic hydrodynamic fields, mass density ρ, fluid velocity u and momentum flux $\boldsymbol{\Pi}$, are moments of the particle distribution function:

$$\rho^* = \sum_i f_i, \quad \rho^* \boldsymbol{u}^* = \sum_i f_i \mathbf{e}_i, \quad \boldsymbol{\Pi} = \sum_i f_i \mathbf{e}_i \mathbf{e}_i \qquad (10\text{-}18)$$

The collision operator is chosen in such a way as to allow the Navier-Stokes equation to be equivalent to equation (10-17) in the appropriate limit. It is assumed that the distribution function f_i is always close to the equilibrium state $f_i^{(eq)}$. The collision operator can then be expressed in terms of the so-called 'collision matrix' M

$$\Omega_i(f_i) = M_{ij}\left(f_j - f_j^{(eq)}\right) \qquad (10\text{-}19)$$

The particle distribution is furthermore assumed to relax to the equilibrium state with a single relaxation time τ^* /Bhatnagar et al 1954/, as well as being isotropic

$$M_{ij} = -\frac{1}{\tau^*}\delta_{ij} \qquad (10\text{-}20)$$

This is called the Bhatnagar-Gross-Krook (BGK) collision matrix and its implications have been widely studied (see for example /Chen & Doolen 1998/). Inserting the BGK operator back into the lattice-Boltzmann equation leads to the famous LBGK evolution equation

$$f_i(\boldsymbol{r} + \mathbf{e}_i, t+1) = f_i(\boldsymbol{r}, t) - \frac{1}{\tau^*}\left[f_i(\boldsymbol{r}, t) - f_i^{(eq)}(\boldsymbol{r}, t)\right] \qquad (10\text{-}21)$$

Various macroscopic parameters are identified. The relaxation time τ^* in equation (10-21) is related to the kinematic viscosity γ^* as

$$\gamma^* = \beta\left(\tau^* - \frac{1}{2}\right) \qquad (10\text{-}22)$$

where β is a constant that is dependent on the geometrical details of the lattice (hexagonal, square, or cubic, /Succi 2001/). Physically realistic, positive kinematic viscosities are obtained for relaxation times that satisfy $\tau^* > 1/2$.

The fluid pressure is given by

$$P(\boldsymbol{r}, t) = c_s^2\left(\rho(\boldsymbol{r}, t) - \overline{\rho}\right) \qquad (10\text{-}23)$$

where $\overline{\rho}$ is the mean density of the fluid and c_s is the speed of sound.

In this study high Reynolds number flow is of interest. In the simulation care has to be taken of high Reynolds number (turbulent) flows to ensure a fine enough grid to resolve the short scale structure.

Quantities	LBGK parameters	Physical parameters
Speed of sound	c_s^*	$c_s = \dfrac{\Delta r}{\Delta t} c_s^*$
Density	$\rho^* = \sum_i f_i$	$\rho = \dfrac{\Delta m}{\Delta r^3} \rho^*$
Velocity	$u^* = \dfrac{1}{\rho} \sum_i f_i e_i$	$u = \dfrac{\Delta r}{\Delta t} u^*$
Viscosity	$\gamma^* = \dfrac{1}{6}\left(2\tau^* - 1\right)$	$\gamma = \dfrac{\Delta r^2}{\Delta t} \gamma^*$
Pressure	$P^* = \left(c_s^*\right)^2 \rho^*$	$P = \dfrac{\Delta m}{\Delta r \Delta t^2} P^*$

Tabelle 10.1 Conversion rules for LBGK quantities and their corresponding physical values.

10.4 Boundary conditions

In this section the boundary conditions are put forward for the flow problem in both open water and coarse layer regions. There are two conditions that require specification: (a) solid fluid boundary conditions and (b) conditions on the outside of the region as a whole.

For (a) the no-slip boundary condition must be made relevant to the lattice-Boltzmann method. This is done by ensuring that no fluid particle can flow into the wall.

The node points that most closely approximate the wall surface are treated in a special manner. Following /Ladd 1994/ the fluid inside the wall is given a very high mean mass density. Therefore, the collision between fluid particles inside and outside the wall is such that the fluid particles in the fluid region appear to bounce back. This procedure is equivalent to the continuum no-slip condition.

For (b) various approximations are introduced. The bottom of the coarse layer requires a suitable boundary condition. Essentially a slipping boundary condition for the tangential velocity component is appropriate, see /Saffmann 1971/ and /Beavers & Joseph 1967/. This condition reads for the slip velocity

$$u_s = -L_s \frac{\partial u}{\partial y} \qquad (10\text{-}24)$$

where the slip length L_s is related to the geometric permeability k_g of the subsoil as

$$L_s = \frac{\sqrt{k_g}}{\alpha}. \qquad (10\text{-}25)$$

The geometric permeability is related to the engineering permeability as $k_g = \mu k / \gamma_w$, where μ is the viscosity of the fluid. /Saffman 1971/ uses $\alpha \approx 0.1$. The geometric permeability k_g has the form $k_g = d^2 / c$, with c a porosity dependent constant, and d the mean particle diameter of the subsoil. In practice d is so small that L_s is zero and the no-slip condition holds. The normal velocity u_n is in principle related to the solution of the pressure in the subsoil. In practice, the approximation $u_n = 0$ may be introduced.

For the flow in the open water region, far from the obstacle, two different velocity profiles have been applied; logarithmic velocity and wave loading.

10.5 Flow with logarithmic velocity profile

The flow in the open water region is expected to display a logarithmic velocity profile with respect to the x-direction. In this direction periodic boundary condition are enforced. At the top of this region a constant velocity U is prescribed.

The logarithmic velocity distribution becomes invalid in the laminar sub-layer, which has height y. In this sub-layer, which is very thin compared to the dimension of the whole problem, and chosen to be equal to half of the mean coarse particle diameter, a linear velocity profile is imposed. The latter vanishes at the top of the coarse layer; a zero value is also introduced on the sides of the coarse layer in the region $0 \leq y \leq y_0$, see Bild 10-3.

The logarithmic velocity profile for $y > y_0 + \delta$ is expressed in the Karman constant b, the velocity parameter u_0 and the sub-layer thickness δ , see /Landau & Lifshitz 1959/,

$$u = \frac{u_0}{b\delta}(y - y_0), \qquad y_0 < y \leq y_0 + \delta \qquad (10\text{-}26)$$

$$u = \frac{u_0}{b}\ln\left(\frac{y - y_0}{\delta} e\right), \qquad y > y_0 + \delta \qquad (10\text{-}27)$$

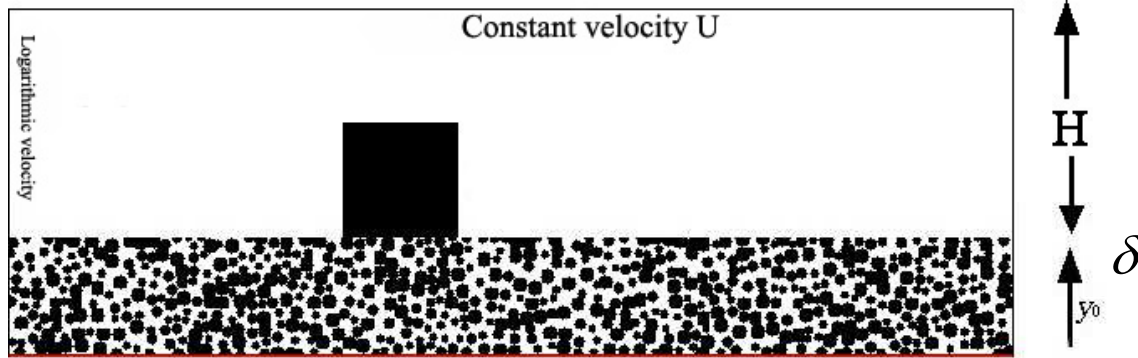The velocity at the top of the open water region $y = H + y_0$

Bild 10.3   *The height of the system is* $H + y_0$ *, and* δ *is the viscous sub-layer length. A logarithmic velocity profile has been imposed on the left side of the system and a*

is

$$U = \frac{u_0}{b} \ln\left(\frac{He}{\delta} \right) \tag{10-28}$$

The velocity parameter u_0 is thus related to the velocity at the top of the open water region as

$$u_0 = \frac{bU}{\ln\left(\dfrac{He}{\delta} \right)} \tag{10-29}$$

All these boundary conditions are implemented in the lattice-Boltzmann procedure. The control variable that ultimately defines the velocity field in the open water and coarse layer region is the constant velocity at the top U.

Everything else depends on the details of the geometry. While there is considerable time-dependence in the flow field, these experiments will be called *steady flow experiments*, because there is no explicit temporal loading.

10.6 Wave loading flow

In these experiments there is explicit time-dependence in the external forcing of the flow. The flow in the open water region is prescribed as a wave velocity profile in the vertical y-direction. Periodic boundary condition is enforced in the x-direction.

A simple oscillation in the y-direction with frequency ω and amplitude L can be written as a function of time t and horizontal position x as

$$y(x) = H + L \sin\left(\frac{2\pi x}{\lambda} \right) \cos(\omega t) \tag{10-30}$$

where $\omega = 2\pi f$.

Therefore, the wave velocity vector at the top of the open region is

$$\left(0, -L\omega \sin\left(\frac{2\pi x}{\lambda} \right) \sin(\omega t) \right) \tag{10-31}$$

The wavelength λ is chosen in such a way that it fits the size of the problem exactly, which is necessary to satisfy the periodic boundary conditions.

The numerical values of the wave loading parameters are presented in Tabelle 10-2. In addition to simple wave loading, a loading programme that combines waves with steady velocity is also possible.

10.7 Results of the simulations

The table below summarises the details of the geometries and the velocity profiles of the various simulations. The results of the simulated tests are presented as follows. The flow in the open water and coarse granular layer is demonstrated by means of a single snapshot (though cartoon sequences of the simulations are available).

The excess pore pressure distribution in the subsoil is shown as a sequence of snapshots, as the temporal development of this parameter is obviously the key to obtaining the location where erosion due to gas is most likely to occur.

10.7 Steady flow simulations (tests 1 & 2)

The results of tests 1 and 2 (see Tabelle 10-2) turn out to be very similar, despite the difference in loading speed. Eddies are generated downstream from the obstacle. A snapshot of the calculated flow pattern is shown in Bild 10- 4.

The mean size is of the same order of magnitude of the height of the obstacle. The excess pore pressure is shown in Bild 10-5, also for test number 1.

Test no.	Type of test	Flow parameters	Gravel layer thickness $y_0\,(m)$	Water level $H\,(m)$	Mean gravel size $d\,(m)$	Obstacle height × width $(m{\times}m)$
1	Steady flow	$U = 0.08\ \mathrm{ms^{-1}}$	0.018	0.1	0.005	0.05 × 0.02
2	Steady flow	$U = 0.29\ \mathrm{ms^{-1}}$	0.1	0.2	0.01	0.1 × 0.11
3	Wave loading	$\lambda = 0.29\ \mathrm{m}$ $f = 1.0\ \mathrm{s^{-1}}$	0.1	0.2	0.01	none
4	Wave loading	$\lambda = 0.29\ \mathrm{m}$ $f = 1.0\ \mathrm{s^{-1}}$	0.1	0.2	0.01	0.1 × 0.1
5	Wave loading	$\lambda = 0.29\ \mathrm{m}$ $f = 1.0\ \mathrm{s^{-1}}$	0.04	0.16	0.01	0.04 × 0.06
6	Wave loading	$\lambda = 0.29\ \mathrm{m}$ $f = 1.0\ \mathrm{s^{-1}}$	0.1	0.4	0.01	none

Tabelle 10.2   Details of the simulated tests. The subsoil has a permeability

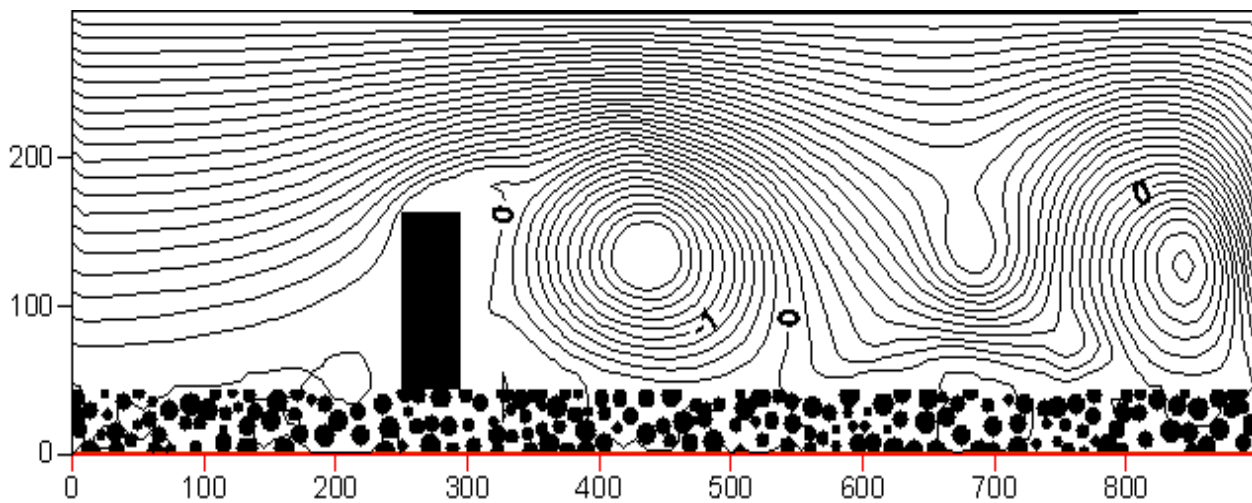$$k = 4\times10^{-4}\ ms^{-1}\ \text{and the saturation is}\ \ s_i = 0.95.$$

Bild 10.4   Snapshot of the flow pattern of test number 1.

The region that experiences the greatest risk of being damaged by oscillatory pore water flows is located at $400 < x < 600$ (lattice units), in other words in the region between one and two obstacle heights downstream from the obstacle.

10.8 Wave loading with no obstacle (test 3 & 6)

Three waves with wave length 0.29 m have been imposed at each time step. A snapshot of the flow pattern of test 3 is shown in figure 6.

In this simulation the flow is caused by the vertical wave bouncing back from the gravel, while at the same time dispersion is displayed. The same phenomenon is observed in test 6, though in this test the water depth was greater, thus ameliorating the dispersion phenomenon. From the animation of the pressure in the subsoil (see Bild 10-7) it is seen that the pressure oscillates in harmony with the wave. This is expected. As result the excess pore pressure gradient will oscillate too, which may cause erosion in the subsoil. The potentially most damaged locations appear at about   and   , in sympathy with the applied wave and extending to about half the wavelength.
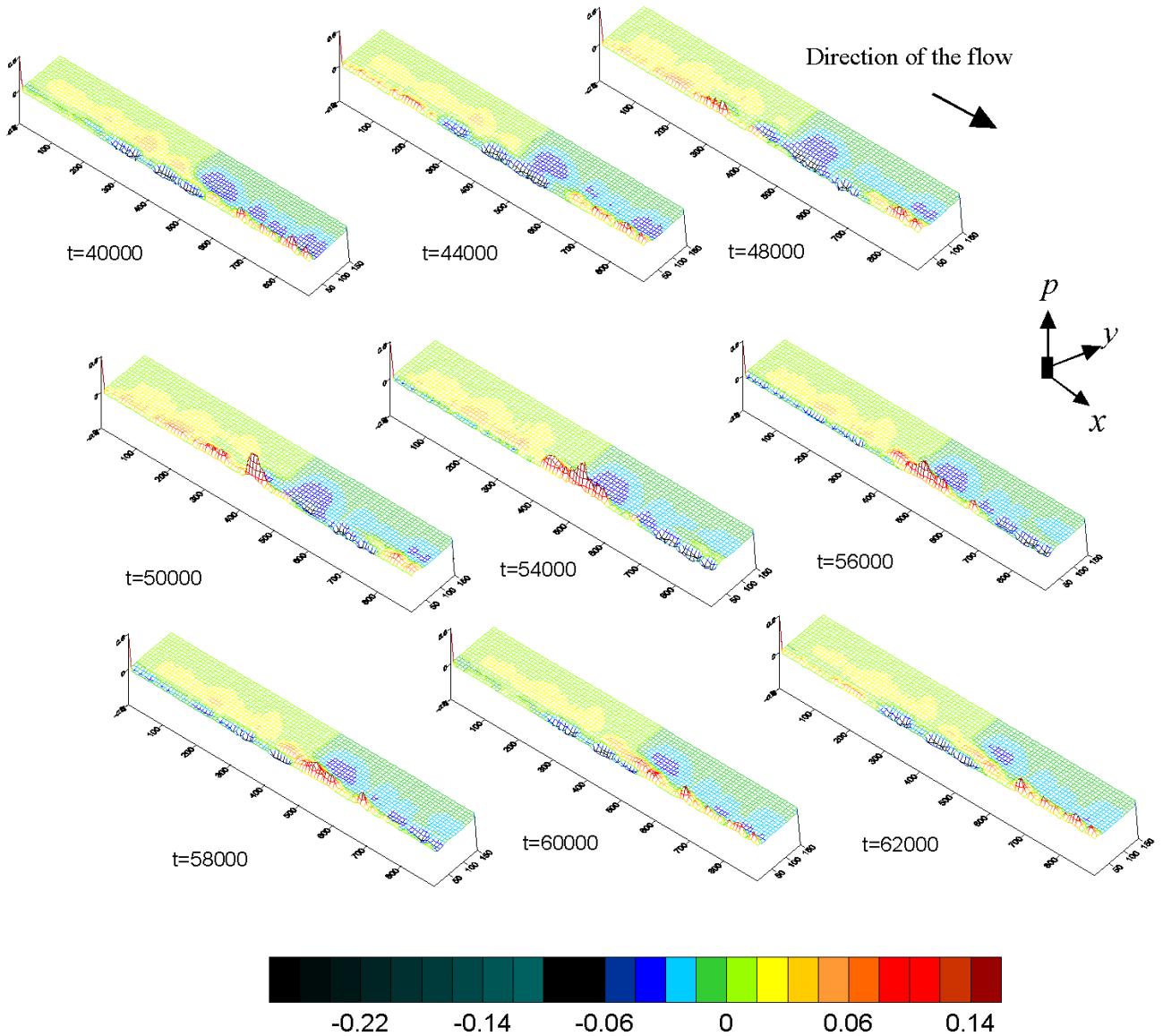
Bild 10.5   *Sequence of snapshots of the excess pore pressure in the subsoil for steady flow. The areas with the greatest colour variation are most at risk from erosion.*
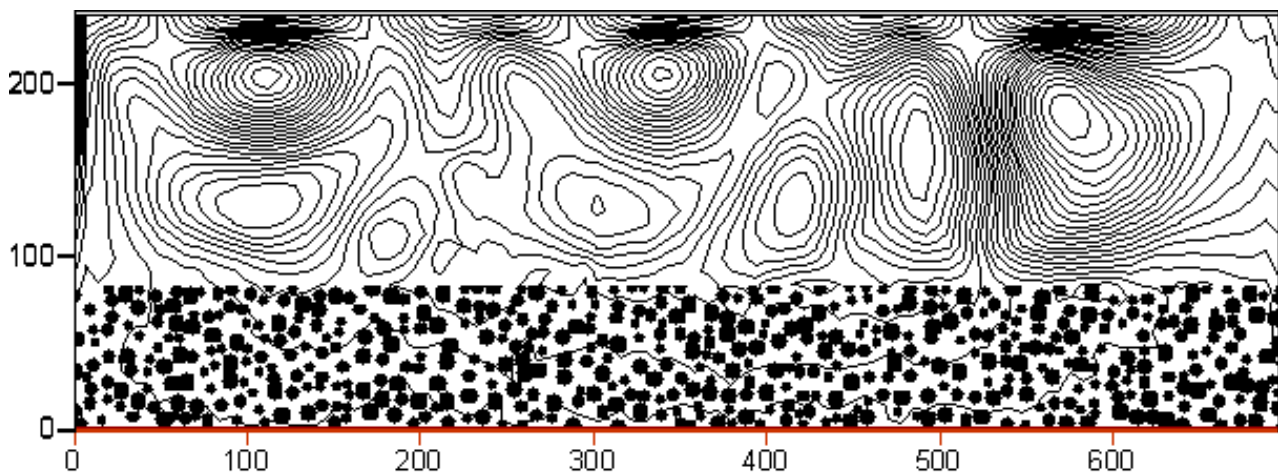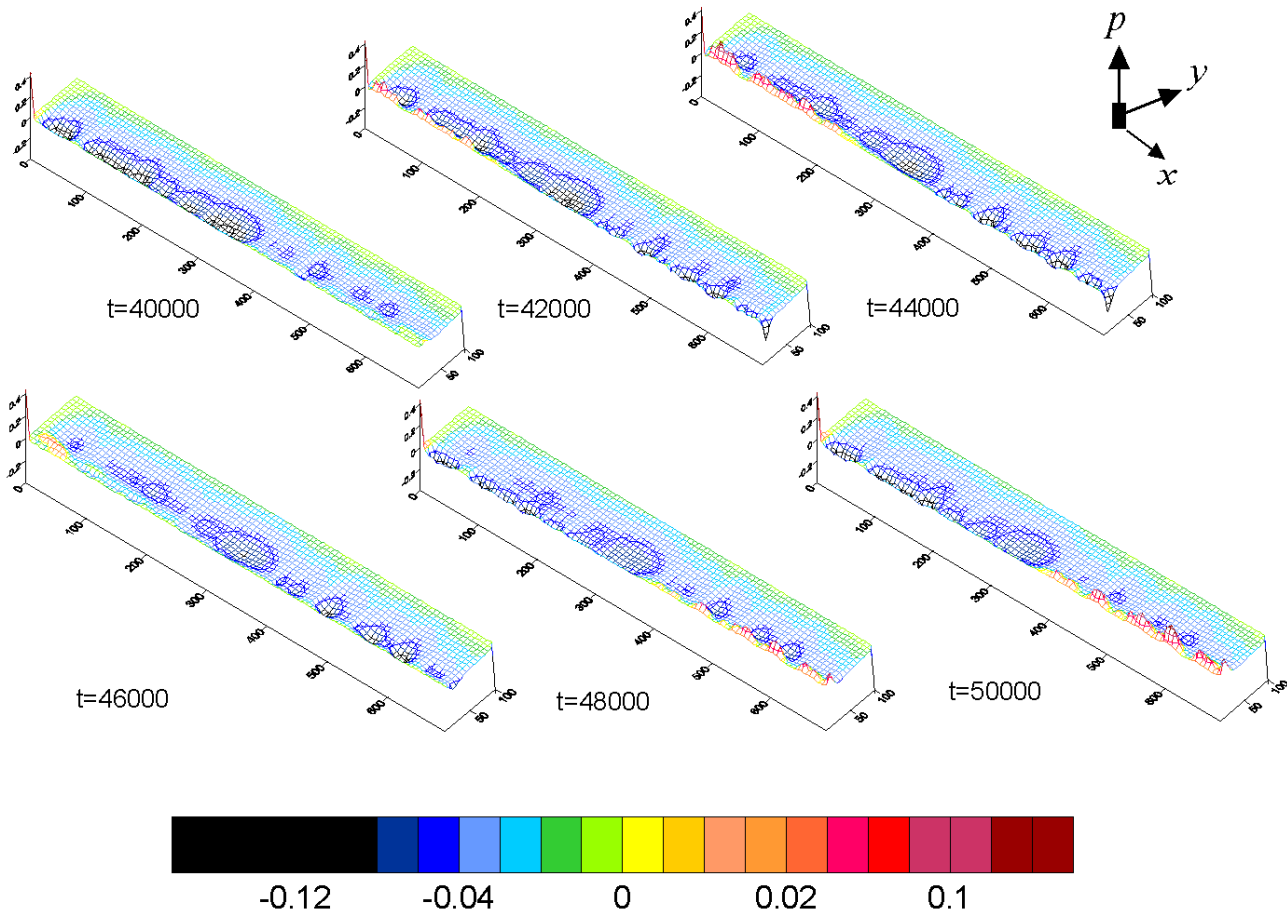

Bild 10.6   *Snapshot after 70,000 time steps of the flow lines as a function of the position for the case of wave loading with no obstacle flow.*

Bild 10.7   Sequence of snapshots of the excess pore pressure in the subsoil for wave loading in the absence of an obstacle. The areas with the greatest colour variation are most at risk from erosion.

Here, 10,000 time steps in the simulation correspond to 0.8 seconds in real time.

In test number 6 the damping of the wave is so severe that only very small pressure fluctuations are observed and these are not reported separately.

10.8 Wave loading with an obstacle (test 4 & 5)

The simulation of the wave loading flow over an obstacle with a height of 0.1 m has been carried out with a wavelength of the free surface flow of 0.29 m. In this experiment eddies are generated as a result of the presence of the obstacle.

This is a very complex flow pattern; a snapshot is shown in Bild 10-8. The result is roughly the same for both tests and therefore only test number 4 is shown. The size of the eddies is of the order of the height of the obstacle.

Bild 10-9 shows the associated excess pore pressure in the subsoil. The presence of the obstacle has the effect of attracting damage. The location of

the regions that are most at risk are just in front and just behind the obstacle: the obstacle itself occupies the region $232 < x < 312$.

10.9 Conclusions

These two-dimensional simulations need to be compared with real experimental data. The results are indicative, as real flow situations will be three-dimensional and turbulence is a three dimensional phenomenon. Nonetheless, indications of the likely locations of damage-susceptible regions, associated with gas in the subsoil, is useful.

For the steady flow problem over an obstacle the most likely location is some two obstacle heights downstream. For wave loading without an obstacle, it is directly associated with the troughs and crests of the waves, but only in shallow water. For wave loading in the presence of an obstacle the region of potential greatest damage is on either side of the object and the risk of erosion here is enhanced compared to wave loading in the absence of an alien object.
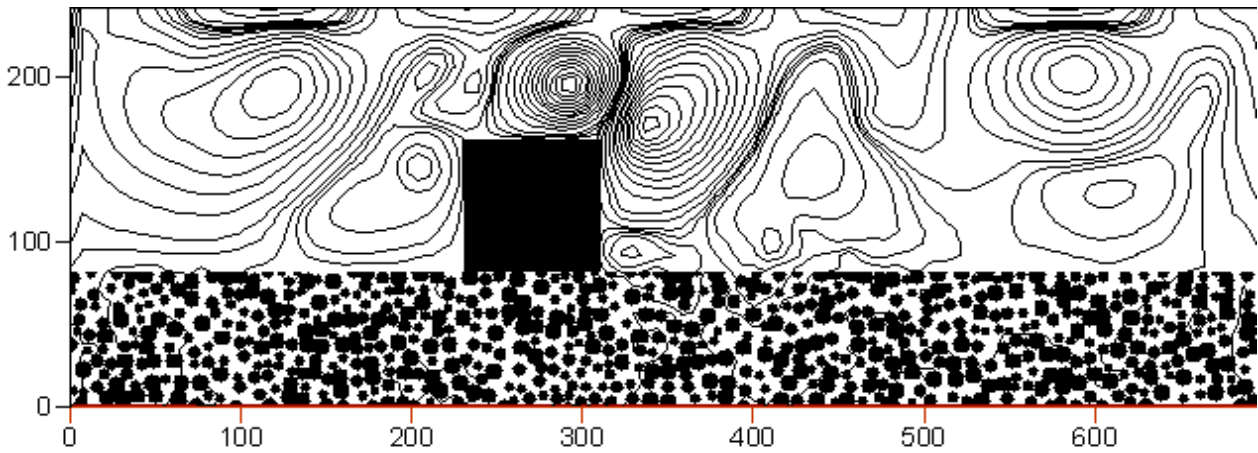
Bild 10.8   Stream lines for the fluid flow around an obstacle in wave loading at the time point of 41,000 time steps (4 seconds into the simulation with a wave of a duration of 1 s).
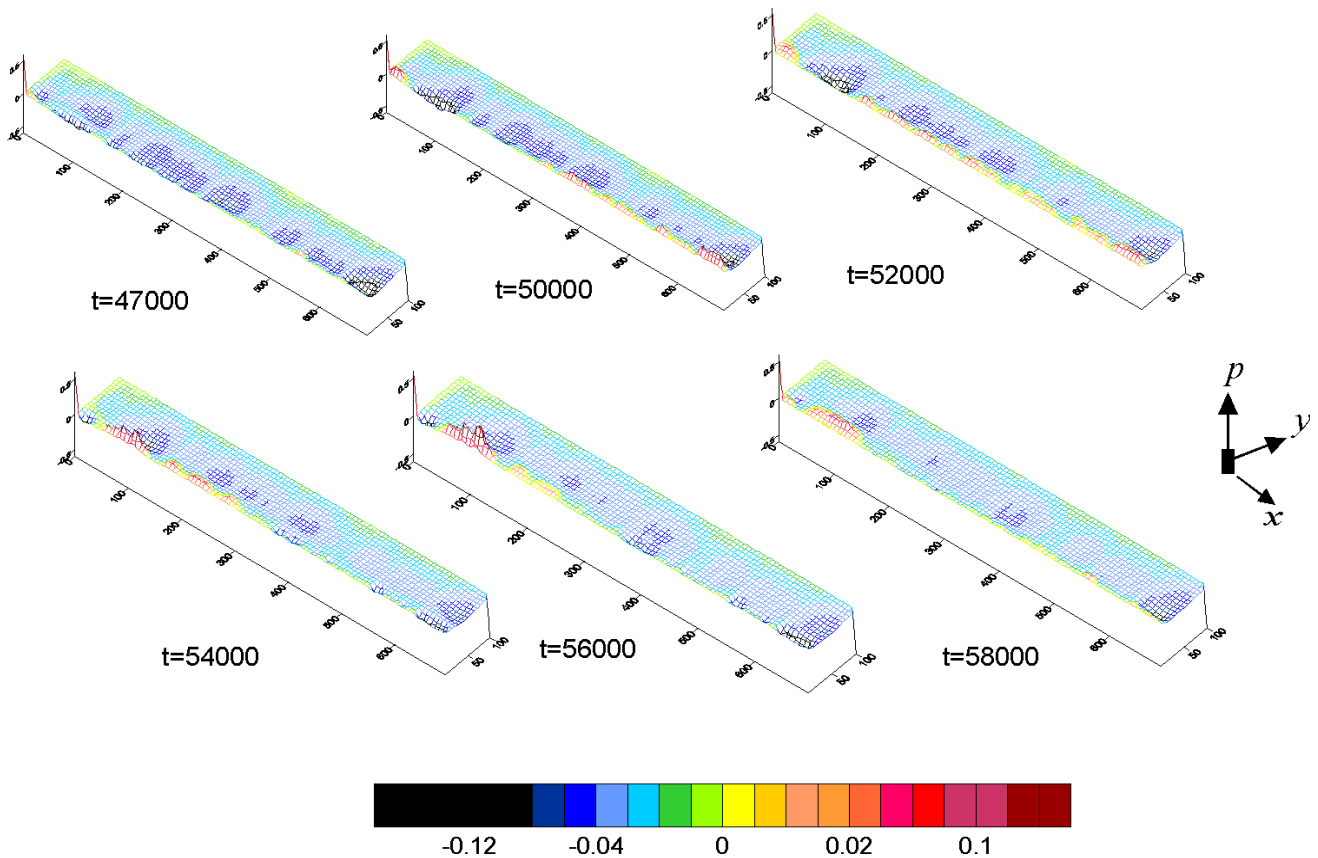

Bild 10.9   Subsoil excess pore pressure for wave loading with an obstacle. The regions where the greatest damage potentially takes place is just before and behind the obstacle.

10.10 Acknowledgements

10.11 List of symbols

a	$\sqrt{4n(1-s_i)/k}$
A	consolidation coefficient ($m^2 s^{-1}$)
b	Karman constant (-)

c	porosity-dependent coefficient (-)		y_0	thickness of the gravel layer (m)
c_s	speed of sound (ms^{-1})		Y	pressure-equivalent water depth (m)
c_s^*	scaled speed of sound (-)		α	coefficient for slipping boundary condition (-)
d	diameter of subsoil grain (m)		β	lattice-geometry-dependent coefficient (-)
e_i	unit vector (-)		γ^*	scaled kinematic viscosity (-)
f	frequency (s^{-1})		γ_w	unit weight of water (Nm^{-3})
f_i	particle distribution function (-)		δ	thickness of the laminar sub-layer (m)
f_i^{eq}	euilibrium distribution function		δ	Kronecker delta (-)
i_c	critical gradient (-)		Δm	mass of fluid particle (kg)
H	fluid height of open water (m)		Δr	lattice spacing (m)
k	engineering permeability (ms^{-1})		Δt	time step (s)
k_g	Geometric permeability (m^2)		χ	Fourier wave number (m^{-1})
L	amplitude of applied wave (m)		λ	wavelength (m)
L_s	slip length (m)		μ	fluid viscosity (Pas)
M	number of temporal points (-)		ω	circular frequency (s^{-1})
M	collision matrix (-)		Π	scaled momentum flux (-)
n	porosity (-)		Ω_i	collision operator (-)
N	number spatial points on the interface (-)		ρ	fluid density (kgm^{-3})
$\overline{N}$	number of lattice points in the simulation (-)		ρ^*	scaled fluid density (-)
p	excess pore pressure (Pa)		$\overline{\rho}$	mean density of the fluid (-)
p_0	ambient pressure (Pa)		$\dot{\sigma}$	rate of pressure fall (Pas^{-1})
P	total fluid pressure (Pa)		τ	time (s)
r	location vector (m)		τ^*	scaled relaxation time (-)
s	Laplace frequency (s^{-1})		ξ	position (m)
s_i	saturation (-)		ζ	$4A\tau/y^2$ (-)
t	time (s)		λ	wavelength (m)
t_1	duration of pressure fall (s)			
u	velocity vector (ms^{-1})			
$\boldsymbol{u}^*$	scaled velocity vector (-)			
u_0	velocity outside laminar sub-layer (ms^{-1})			
u_n	normal velocity (ms^{-1})			
u_s	slip velocity (ms^{-1})			
U	velocity at the top of the simulation for steady flow (ms^{-1})			
x	horizontal position co-ordinate (m)			
y	vertical position co-ordinate (m)			

10.12 References

Abramowitz, M., Stegun, I.A. 1965

Handbook of mathematical functions Dover, New York.

Beavers, G. S. and Joseph, D. D. 1967

Boundary condition at a naturally permeable wall, Journal of Fluid Mechanics, Vol. 30, part 1: 197-207

Bhatnagar PL, Gross E.P. and Krood, M. 1954

A model for collision processes in gases. I: small amplitude processes in charged and neutral one-component system, Phys. Rev. 94:511-525

Biot, M.A. 1941
General theory of three dimensional consolidation, J. Appl. Physics, 12, 155-164.

Chen, S. and Doolen, G. 1998
Lattice Boltzmann method for fluid flows, Annu. Rev. Fluid Mech., 30: 329-364.

Chopard, B. and Droz, M. 1998
Cellular Automata Modelling of Physical System, Cambridge University Press

Gradshteyn, L.S. and Ryzhik, L.M. 2000
Table of integral series and products (6th ed) Academic Press London

Köhler, H.J. and Koenders, M. A. 2003
Direct visualisation of underwater phenomena in soil-fluid interaction and analysis of the effects of an ambient pressure drop on unsaturated media, Journal of Hydraulic Research, 41 (1), 69-78.

Ladd, A. J. C. 1994
Numerical simulations of particulate suspensions via a discretized Boltzmann equation. Part 1. Theoretical foundation, J. Fluid Mech. 271, 285-309; Part 2. Numerical results, J. Fluid Mech. 271, 311-339.

Landau, L.D. and Lifshitz, E. M. 1959
Fluid Mechanics, Pergamon, Oxford

Raudkivi, A.J. 1998.
Loose boundary conditions. Rotterdam, Balkema

Roussel, N., Köhler, H. J. and Koenders, M. A. 2000
Analysis of erosion protection measures in partially saturated subsoils, Filter and drainage in geotechnical and environmental engineering (eds Wolski, E. and Mlynarek, J.) Balkema Rotterdam, 75-82.

Saffmann, P. G. 1971.
On the boundary condition at the surface of a porous medium, Studies in Applied Mathematics, L (2)

Succi, S. 2001
The Lattice Boltzmann equation for fluid dynamics and beyond, Clarendon press. Oxford

Terzaghi. K. (1943)
Theoretical soil mechanics, Wiley, New York.